



HAL
open science

Bayesian image restoration for mosaic active imaging

Nicolas Lermé, François Malgouyres, Dominique Hamoir, Emmanuelle Thouin

► **To cite this version:**

Nicolas Lermé, François Malgouyres, Dominique Hamoir, Emmanuelle Thouin. Bayesian image restoration for mosaic active imaging. 2013. hal-00758753v2

HAL Id: hal-00758753

<https://hal.science/hal-00758753v2>

Submitted on 25 Jul 2013 (v2), last revised 18 Apr 2014 (v3)

HAL is a multi-disciplinary open access archive for the deposit and dissemination of scientific research documents, whether they are published or not. The documents may come from teaching and research institutions in France or abroad, or from public or private research centers.

L'archive ouverte pluridisciplinaire **HAL**, est destinée au dépôt et à la diffusion de documents scientifiques de niveau recherche, publiés ou non, émanant des établissements d'enseignement et de recherche français ou étrangers, des laboratoires publics ou privés.

Bayesian image restoration for mosaic active imaging

Nicolas Lermé*, François Malgouyres†, Dominique Hamoir‡
Emmanuelle Thouin§ ¶ ||

May 11, 2013

Abstract

In this paper, we focus on the restoration of images acquired with a new active imaging concept. This new instrument generates a mosaic of active imaging acquisitions. We first describe a simplified Bayesian model of this so-called “mosaic active imaging”. We also assume a prior on the distribution of images, using the total variation, and deduce a restoration algorithm. This algorithm iterates one step for the estimation of the restored image and one step for the estimation of the acquisition parameters. We then provide the details useful to the implementation of these two steps. In particular, we show that the image estimation can be performed with graph-cuts. This allows a fast resolution of this image estimation step. We give detailed numerical experiments. They show that acquisitions made with a mosaic active imaging device can be restored even under severe noise levels.

Keywords: graph-cut, active imaging, laser imaging, image reconstruction, image estimation.

1 Introduction

Flash laser imaging, also called flash active imaging, gated active viewing, or more commonly active imaging, illuminates the object to be observed with a very short laser flash (of typically 5-20 ns). It captures the image with a high-speed camera, sharply synchronized with the emission. The photons coming back to the sensor are selected according to their round-trip travel time. This permits to eliminate the photons back-scattered by the foreground (e.g. by fog, dust or vegetation) and those back-scattered by the background. The controlled addition of photons and their temporal selection allow a better signal to noise ratio and a better contrast of the object over the background. It is of interest for surveillance and for target identification under bad weather conditions or at long ranges (several kilometers).

*Institut Supérieur d'Électronique de Paris, Paris, France, nicolas.lerme@isep.fr

†IMT-UMR5219, Université de Toulouse, CNRS, Toulouse, France, francois.malgouyres@math.univ-toulouse.fr

‡ONERA - The French Aerospace Lab, F-31055 Toulouse, France, dominique.hamoir@onera.fr

§ONERA - The French Aerospace Lab, F-31055 Toulouse, France, emmanuelle.thouin@onera.fr

¶Université de Toulouse, Institut Supérieur de l'Aéronautique et de l'Espace (ISAE), F-31055 Toulouse

||IMT-UMR5219, Université de Toulouse, CNRS, Toulouse, France.

A discrimination in sub-meter distance can be obtained in some cases. The observed objects typically have metric dimensions (e.g. buildings, vehicles, personnel, animals, fences). Depending on the application, they are located at distances from the imaging system ranging from 10m to 20km. In the most demanding applications, including those requiring distances in kilometers, several physical limitations degrade the images [HVB⁺09, RHV⁺09].

First, atmospheric turbulence produces two types of degradation. On the one hand, the laser illumination is not uniform over the object and is not stationary due to the forward propagation of the laser beam through the turbulent atmosphere. We talk of turbulence-induced illumination speckle (also speckle). On the other hand, the image of the object is distorted by the backward propagation.

Second, the interaction of the laser spot with the object is accompanied by artifacts, in particular if the light may be multiply scattered off several surfaces (e.g. the inner side of a dihedral).

Third, the maximum distance of observation is limited by the size, weight and power compatible with integration on a land or air vehicle, in particular that of the laser and that of the reception optical system. A first way to overcome this difficulty is to restore the information despite a low signal to noise ratio (currently of a few units). A second way is to improve the light sensor, for instance in switching to avalanche photodiodes (APD). A third approach is to restore the image from a mosaic of typically 100 to 1,000 elementary thumbnails [Ham10]. In the latter case, that we will call mosaic laser imaging or mosaic active imaging, each thumbnail has strong gradients of illumination, and geometric readjustments may have to be considered. This is the option studied in this paper.

In order to restore the observed scene from the mosaic of images, we adapt well known strategies of image processing. In particular, we use the prior that images have a small total variation (TV). This prior has first been proposed for image denoising (see [ROF92]) and has, since then, been applied in many contexts of image restoration such as deblurring, inpainting, image zooming, restoration of compression artifacts, etc. Beside its ability to properly restore images, its minimization has been studied intensively, and fast and simple iterative algorithms have been developed (see, for instance, [Cha04, BBFAC04]). More recently algorithms using graph-cuts have been developed and provide fast minimization methods for some models involving this prior (see [Cha05, DS04, DS06, CD09]).

In this paper, we investigate algorithmic ways to restore mosaic active images (the third approach above). The rest of this paper is organized as follows. In Section 2, we describe a simplified physical and mathematical model of the imaging process and describe the sketch of the restoration algorithm. In particular, this section exhibits that the image acquisition depends on imperfectly known acquisition parameters. The algorithm consists in alternating the estimation of these acquisition parameters and the estimation of the image. Next, we show in Section 3 how the estimation of the image can be formulated using level-sets and solved with graph cuts. Then, in Section 4, we give the details concerning the implementation of the algorithm used to estimate the acquisition parameters. **Afterwards**, we provide in Section 5 numerical experiments assessing the quality of the image estimate, the influence of the acquisition parameters, the convergence of the algorithm used to estimate the acquisition parameters and the results of the algorithm. **Finally, we summarize the contributions of this work and conclude with some interesting perspectives.**

2 Modeling of flash laser imaging

2.1 Overview

In flash laser imaging, a “light ball” is repeatedly sent towards the object to be observed. A time-gated camera synchronized with the laser is used to detect and select the light that is received within a brief time-interval or time-gate dt of typically a few nano to micro seconds, after a chosen time delay of typically 10^{-7} to 10^{-4} s has elapsed. This allows to record the photons coming back from the object (in the time-gate) and to reject those coming back from the foreground or from the background (before or after the time-gate). The wavelength of operation can be chosen according to the application but is usually in the so-called eye-safe region, between 1.5 and 1.6 micrometers.

Generally, the field of view of the camera is fully illuminated by the laser and is acquired at standard video rates, say 10 Hz. In mosaic laser imaging, we replace the low-repetition-rate, 10Hz Nd:YAG laser with OPO (Optical Parametric Oscillator) by a high-repetition-rate, 10kHz fiber laser that is expected to offer higher average powers and plug-efficiencies within a few years. This concept presents additional advantages. As the repetition rate is larger by three orders of magnitude, the energy per pulse is lowered by the same ratio. In order to maintain the signal-to-noise ratio, only a reduced part of the field of view is illuminated at each laser flash. The corresponding region of interest of the sensor is read. The laser beam is then deflected in order to illuminate another region of interest. By repeating the process we scan the field of view of the camera. This results in the successive acquisition of elementary images taken at a repetition-rate of 10 kHz that will tile as a mosaic in order to build the full-frame image at 10 Hz. The formation of each elementary image can be modeled as follows.

The object is illuminated with a Gaussian laser spot with nominal position \bar{c}_k in the image and beam radius \bar{w}_k (radius for which the amplitude of the electromagnetic field is reduced by $1/e$, i.e. its intensity is reduced by $1/e^2$ as compared to their maximum values, e referring to the exponential). This laser spot is affected by three perturbations due to pointing discrepancies and to the forward propagation of the laser beam through the inhomogeneous turbulent atmosphere: beam spreading, beam wandering, and turbulence-induced speckle. This illumination pattern is multiplied by the reflectance of the object to form a luminance distribution. This travels through the atmosphere and is captured by the optical system of the camera to form an image next to its focal plane. Shot noise and thermal noise are then added to the image. This is repeated for each elementary image (the images are indexed by k).

We denote, for an integer $N > 0$, the set of all pixels by $\mathcal{P} = \{1, \dots, N\}^2$. We denote $K \geq 1$, the number of elementary images. For every index $k \in \{1, \dots, K\}$, the image $(v_p^k)_{p \in \mathcal{P}} \in \mathbb{R}^{\mathcal{P}}$ is obtained from the object $(u_p)_{p \in \mathcal{P}} \in \mathbb{R}^{\mathcal{P}}$, using

$$v_p^k = u_p G_{\theta_k}(p) S_p^k + n_p^k, \quad \forall p \in \mathcal{P},$$

where $\theta_k = (c_k, w_k) \in \mathbb{R}^2 \times \mathbb{R}^*$ contains the parameters of the Gaussian profile, and where the beam intensity profile G_{θ_k} is defined for every $p \in \mathcal{P}$ by

$$G_{\theta_k}(p) = \exp\left(-\frac{\|p - c_k\|^2}{2w_k^2}\right), \quad (1)$$

FIGURE À METTRE ICI

Figure 1: Illustration of the acquisition process.

the speckle pattern $(S_p^k)_{p \in \mathcal{P}} \in \mathbb{R}^{\mathcal{P}}$ and the noise $(n_p^k)_{p \in \mathcal{P}} \in \mathbb{R}^{\mathcal{P}}$.

The mathematical developments will be conducted on elementary images synthesized with this simplified model. We are aware that this model does not take into account neither the size of the reception pupil of the instrument nor the transverse sampling by the focal plane array. Leaving these degradations aside permits indeed to use faster and more efficient restoration algorithms. More precisely, improving the image creation model would force us to use less efficient algorithms whose convergence will be imperfect while requiring more computational resources. We therefore leave the study of this more accurate degradation model, the development of adapted restoration algorithms, as well as the comparison of the two degradation model/algorithm couples for a future work.

The illumination speckle factor (S_p^k) is a colored noise that can be viewed as a textured illumination. It is a strong limitation in terrestrial applications but is negligible in airborne applications. We neglect this possible contribution in this first study and leave it for the near future.

2.2 Beam spreading

The Gaussian beam does naturally spread along the propagation. We denote the distance between the laser source and the object by $d > 0$. The minimum beam radius, at the laser source in our case, is called the beam waist radius and is denoted w_0 . In the absence of atmospheric turbulence, the spreading is only due to the diffraction of the beam:

$$w_{diff}^2 = \left(\frac{\lambda d}{\pi w_0} \right)^2 + w_0^2,$$

where $\lambda > 0$ is the laser wavelength. We propose to model the further beam spreading induced by the atmospheric turbulence by introducing a deviation term dw_k that follows a Gaussian distribution with zero mean and standard deviation σ_w . The radius of the Gaussian beam then writes

$$w_k^2 = \left(\frac{\lambda d}{\pi w_0} \right)^2 + w_0^2 + dw_k^2.$$

In our experimental setup the divergence of the laser beam is 1.08 mrad, corresponding to an expected beam radius of $\bar{w}_k = 16.2$ pixels, as seen by our 256×256 -pixels, 8.5-mrad-field-of-view camera. The standard instrument-to-target range is 1,000 m. The calculated standard deviations of the beam radius are given in Table 1 for standard turbulence levels, defined by their refractive-index-structure constant C_n^2 [Kol49]. Under these conditions, they are very small compared to the mean beam radius and to the pixel size.

2.3 Beam wandering

Beam wandering results from an angular deviation of the beam propagation axis, due to possible pointing discrepancies of the instrument and to the propagation through the turbulent atmosphere.

C_n^2	σ_w
$10^{-15}m^{-\frac{2}{3}}$	6×10^{-4} pixels
$10^{-14}m^{-\frac{2}{3}}$	8×10^{-3} pixels
$10^{-13}m^{-\frac{2}{3}}$	7×10^{-2} pixels

Table 1: Standard deviations of the beam radius w_k , in pixels.

C_n^2	σ_c
$10^{-15}m^{-\frac{2}{3}}$	0.09 pixels
$10^{-14}m^{-\frac{2}{3}}$	0.26 pixels
$10^{-13}m^{-\frac{2}{3}}$	0.81 pixels

Table 2: Standard deviations of the beam position c_k , in pixels.

When considering a perfect pointing, the statistics of this angular deviation respects a Gaussian law with zero mean. Its variance σ_c^2 writes [Fan75, Cha92]

$$\sigma_c^2 = 0.16(\lambda d)^2(2w_0)^{-\frac{1}{3}}r_0^{-\frac{5}{3}},$$

where $2w_0$ is the beam waist diameter and r_0 is the Fried's coherence length of the turbulent atmosphere [Fri66], which is related to C_n^2 [Rod81]. In our example, the calculated standard deviations of the beam position c_k are given in Table 2 for standard turbulence levels.

2.4 Noise

The shot noise or photon noise is due to the statistics of emission of photons by the source. The number of photons, N_p , received by the pixel respects a Poisson's law of expectancy \overline{N}_p and standard deviation σ_p .

The thermal noise or detection noise N_t is a white Gaussian noise with zero mean and standard deviation σ_t . The number of photoelectrons generated in the pixel writes

$$N_e = \eta N_p + N_t,$$

where $0 < \eta < 1$ is the detection efficiency of the sensor.

For low signal levels, the thermal noise dominates over the photon noise. Hence, in the following, we consider additive thermal noise only of normalized standard deviation σ with respect to the maximum intensity of the noise-free image.

2.5 Mathematical modeling and summary of the acquisition process

First, we denote by $\mathcal{N} \subset \mathcal{P}^2$ a neighborhood system connecting pixels. Throughout the paper, we always denote the Euclidean norm $\|\cdot\|$, whatever the dimension of the considered Hilbert space.

We assume that the observed data $u \in \mathbb{N}^{\mathcal{P}}$ is a random variable following a law

$$\mathbb{P}(u) \propto \exp(-\beta TV(u)),$$

where $\beta > 0$ is an unknown parameter (which will later on be tuned by the user) and the total variation TV is defined by

$$TV(u) = \sum_{(p,q) \in \mathcal{N}} d_q^p |u_p - u_q|, \quad (2)$$

where the weights d_q^p are chosen according to [BK05] in order to make the edge capacities crossing any s-t cut in the graph \mathcal{G} a good approximate to the length of an ideal curve.

We also consider $K \geq 1$ and, for every $k \in \{1, \dots, K\}$, parameters $\theta_k = (c_k, w_k) \in \mathbb{R}^2 \times \mathbb{R}^*$ of the Gaussian function G_{θ_k} defined in (1).

When necessary, we denote the coordinates of the elements of \mathbb{R}^2 with subscript i and j (i.e. $c_k = (c_{k,i}, c_{k,j})$ and $p = (p_i, p_j)$).

The random variable c_k is independent of w_k . Their distribution laws are according to

$$\mathbb{P}(c_k) \propto \exp\left(-\frac{\|c_k - \bar{c}_k\|^2}{2\sigma_c^2}\right), \quad \text{for } 1 \leq k \leq K,$$

where $\bar{c}_k \in \mathbb{R}^2$ and $\sigma_c \in \mathbb{R}$ are known parameters and

$$\mathbb{P}(w_k) \propto \exp\left(-\frac{|w_k - \bar{w}_k|^2}{2\sigma_w^2}\right), \quad \text{for } 1 \leq k \leq K, \quad (3)$$

where $\bar{w}_k \in \mathbb{R}^+$ and $\sigma_w \in \mathbb{R}$ are known parameters.

The parameters θ_k are independent random variables. Therefore, their joint distribution satisfies

$$\mathbb{P}((\theta_k)_{1 \leq k \leq K}) \propto \prod_{k=1}^K \mathbb{P}(c_k) \mathbb{P}(w_k).$$

We consider the operator

$$\begin{aligned} M_{(\theta_k)_{1 \leq k \leq K}} : \mathbb{R}^{\mathcal{P}} &\longrightarrow \mathbb{R}^{K\mathcal{P}}, \\ u &\longmapsto ((G_{\theta_k}(p)u_p)_{p \in \mathcal{P}})_{1 \leq k \leq K}. \end{aligned} \quad (4)$$

As already said, we assume that the data $v \in \mathbb{R}^{K\mathcal{P}}$ is obtained by corrupting with an additive white Gaussian noise the observation of an ideal image u through the operator $M_{(\theta_k)_{1 \leq k \leq K}}$. In formula, we have

$$\mathbb{P}(v|u, (\theta_k)_{1 \leq k \leq K}) \propto \exp\left(-\frac{\|M_{(\theta_k)_{1 \leq k \leq K}}u - v\|^2}{2\sigma^2}\right),$$

where $\sigma \in \mathbb{R}$ is the known standard deviation of the noise. Throughout the paper, we denote the components of v with a super script k and have $v = (v^k)_{1 \leq k \leq K}$ with $v^k \in \mathbb{R}^{\mathcal{P}}$.

2.6 Restoration algorithm

Assuming that u is independent of parameters $(\theta_k)_{1 \leq k \leq K}$ and applying Bayes' law, we obtain, for any $v \in \mathbb{R}^{K\mathcal{P}}$, the posterior

$$\begin{aligned} \mathbb{P}(u, (\theta_k)_{1 \leq k \leq K} | v) &= \frac{\mathbb{P}(v | u, (\theta_k)_{1 \leq k \leq K}) \mathbb{P}(u, (\theta_k)_{1 \leq k \leq K})}{\mathbb{P}(v)}, \\ &\propto \exp\left(-\frac{\|M_{(\theta_k)_{1 \leq k \leq K}} u - v\|^2}{2\sigma^2}\right) \exp(-\beta TV(u)) \\ &\quad \times \prod_{k=1}^K \exp\left(-\frac{\|c_k - \bar{c}_k\|^2}{2\sigma_c^2}\right) \exp\left(-\frac{|w_k - \bar{w}_k|^2}{2\sigma_w^2}\right). \end{aligned}$$

We consider in the following a Maximum A Posteriori estimator (MAP) of u and $(\theta_k)_{1 \leq k \leq K}$. **As usual, we compute the MAP estimate by approximately** minimizing in u and $(\theta_k)_{1 \leq k \leq K}$

$$\begin{aligned} -\log(\mathbb{P}(u, (\theta_k)_{1 \leq k \leq K} | v)) &= C + \frac{\|M_{(\theta_k)_{1 \leq k \leq K}} u - v\|^2}{2\sigma^2} + \beta TV(u) \\ &\quad + \sum_{k=1}^K \frac{\|c_k - \bar{c}_k\|^2}{2\sigma_c^2} + \sum_{k=1}^K \frac{|w_k - \bar{w}_k|^2}{2\sigma_w^2}, \end{aligned}$$

where $C \in \mathbb{R}$ does not have any influence on the minimizer.

Given a fixed $v \in \mathbb{R}^{K\mathcal{P}}$, we denote

$$f(u, (\theta_k)_{1 \leq k \leq K}) = \frac{\|M_{(\theta_k)_{1 \leq k \leq K}} u - v\|^2}{2\sigma^2} + \beta TV(u) + \sum_{k=1}^K \frac{\|c_k - \bar{c}_k\|^2}{2\sigma_c^2} + \sum_{k=1}^K \frac{|w_k - \bar{w}_k|^2}{2\sigma_w^2}, \quad (5)$$

for $u \in \mathbb{R}^{\mathcal{P}}$ and $(\theta_k)_{1 \leq k \leq K} \in \mathbb{R}^{3K}$.

It is not difficult to see that, for any $(\theta_k)_{1 \leq k \leq K} \in \mathbb{R}^{3K}$, the function $u \mapsto f(u, (\theta_k)_{1 \leq k \leq K})$ is convex and coercive. It therefore achieves its minimum and one of its minimizers can be computed by standard optimization techniques. When $u \in \mathbb{R}^{\mathcal{P}}$ is fixed, the function $(\theta_k)_{1 \leq k \leq K} \mapsto f(u, (\theta_k)_{1 \leq k \leq K})$ is continuous and coercive. It therefore reaches its minimum. This function is however non-convex and usual optimization algorithms might get stuck in a local minimum. However, when σ_c and σ_w are small enough, we expect this minimum to be close to $(\bar{c}_k, \bar{w}_k)_{1 \leq k \leq K}$.

Notice that considering these properties of f , we cannot a priori provide guarantees that we compute a true minimizer of f . We propose an alternate minimization scheme which is guaranteed to converge to a local minimum. Doing so, we obtain the algorithm described in Table 3. The details of the construction of the two steps of this algorithm are described in Section 3 and Section 4. We will see experimentally that this algorithm has sufficiently good convergence properties in the practical situations we are interested in.

In order to define a stopping criterion, we denote c_i^n , c_j^n and w^n the vectors respectively containing at the iteration n the coordinates of the center and the standard deviation of all Gaussians, i.e. $\forall k \in 1 \leq k \leq K$. The stopping criterion for the loop in n in the algorithm of Table 3 is defined by

$$\|c_i^{n+1} - c_i^n\| + \|c_j^{n+1} - c_j^n\| + \|w^{n+1} - w^n\| \leq \varepsilon_a,$$

where we take $\varepsilon_a = 10^{-2}$.

<ul style="list-style-type: none"> • Initialize $(c_k^0, w_k^0)_{1 \leq k \leq K} = (\bar{c}_k, \bar{w}_k)_{1 \leq k \leq K}$ • Repeat until convergence (loop in n) <ul style="list-style-type: none"> 1. Use a graph cut based algorithm for computing $u^n \in \underset{u \in \mathbb{R}^{\mathcal{P}}}{\operatorname{argmin}} f(u, (c_k^n, w_k^n)_{1 \leq k \leq K}).$ 2. Use a gradient based algorithm to compute $(c_k^{n+1}, w_k^{n+1})_{1 \leq k \leq K} \in \underset{(c_k, w_k)_{1 \leq k \leq K} \in \mathbb{R}^{3K}}{\operatorname{argmin}} f(u^n, (c_k, w_k)_{1 \leq k \leq K}).$

Table 3: Structure of the algorithm used for approximating a minimizer of f .

3 Image estimation using graph cuts

In this section, we first give some reminders about graph cut optimization. Afterward, we recall the model of [ROF92] for image denoising. Then, we briefly explain how the functional f can be formulated into leveled-energies when the parameters $(\theta_k)_{1 \leq k \leq K}$ are known (see the first step of Table 3). Then, we show that this functional has the form of [Cha05] and can therefore be minimized using the same approach.

3.1 Graph cuts framework

Graph cuts are a discrete optimization method able to minimize energies of common computer vision tasks by computing a maximum-flow / minimum-cut in a graph. During about one decade, this method remained bounded to binary image denoising [GPS89] because of limited resources and algorithmic developments. After ten years of silence, graph cuts have progressively emerged as a powerful tool for efficiently solving a wide range of problems: image segmentation, denoising, reconstruction, optical flow, texture synthesis, etc. thanks to a fast maximum-flow algorithm [BK04]. In this framework, we consider the minimization of

$$E(x) = \sum_{p \in \mathcal{P}} E_p(x_p) + \beta \sum_{(p,q) \in \mathcal{N}} E_{p,q}(x_p, x_q), \quad (6)$$

among $x \in \{0, 1\}^{\mathcal{P}}$. As is usual, the unary term $E_p(\cdot)$ in the latter equation is the cost for assigning the label x_p to p independently of its neighbors. The pairwise term $E_{p,q}(\cdot)$ penalizes the pixel pair (p, q) having different labels. The equilibrium between both terms is controlled by the parameter β .

Let us now consider an oriented and capacitated network $\mathcal{G} = (\mathcal{V}, \mathcal{E}, c)$ with a set of nodes $\mathcal{V} = \mathcal{P} \cup \{s, t\}$, a set of edges $\mathcal{E} \subset (\mathcal{V} \times \mathcal{V})$ (corresponding to relations between nodes) and edge capacities $c : (\mathcal{V} \times \mathcal{V}) \rightarrow \mathbb{R}^+$. The extra nodes s and t are called the source and the sink, respectively. We denote by $\mathcal{C} = (\mathcal{S}, \mathcal{T})$ an s-t cut which is a partition of the set of nodes \mathcal{V} where we impose that $s \in \mathcal{S}$ and $t \in \mathcal{T}$. For any s-t cut \mathcal{C} , we define its value in the graph \mathcal{G} by

$$\operatorname{val}_{\mathcal{G}}(\mathcal{C}) = \sum_{(p,q) \in (\mathcal{S} \times \mathcal{T})} c(p, q).$$

Given an s-t cut \mathcal{C} , we also define a binary solution $x^{\mathcal{C}} \in \{0, 1\}^{\mathcal{P}}$ with

$$x_p^{\mathcal{C}} = \begin{cases} 0 & \text{if } p \in \mathcal{T} \\ 1 & \text{if } p \in \mathcal{S} \end{cases}, \quad \forall p \in \mathcal{P}. \quad (7)$$

One can easily see that the application $\mathcal{C} \rightarrow x^{\mathcal{C}}$ makes a one-to-one correspondence between s-t cuts and segmentation of the pixels. The core of graph cuts is then to set the edge capacities in the graph \mathcal{G} such that

$$\text{val}_{\mathcal{G}}(\mathcal{C}) = E(x^{\mathcal{C}}) + C,$$

where the constant C is irrelevant in the context of minimization. This is possible as soon as pairwise terms $E_{p,q}(\cdot)$ are submodular, i.e. when they satisfy for all pixel pairs

$$E_{p,q}(0, 0) + E_{p,q}(1, 1) \leq E_{p,q}(0, 1) + E_{p,q}(1, 0). \quad (8)$$

In this case, the graph \mathcal{G} can be constructed as described in [KZ04] to obtain an optimal labeling of u . As a consequence, the s-t cut of minimum weight (i.e. the s-t minimum-cut) in the graph \mathcal{G} is guaranteed to correspond to a global minimizer of (6) [KZ04]. The s-t minimum-cut of a graph can be found in polynomial time of the number of nodes $\#\mathcal{V}$ and edges $\#\mathcal{E}$ using an efficient maximum-flow algorithm such as [BK04]. In practice, most of these algorithms give near-linear complexity (with respect to the image size) on typical computer vision problems (see [BK04]), including image denoising.

3.2 Level-sets reformulation

Since two decades, Total Variation (TV) regularization has been extensively studied and used in digital image processing due to its ability to accurately preserve sharp edges in images. TV-based models are very popular in the image processing community (see [ROF92] and the papers referencing it). The model proposed by Rudin-Osher-Fatemi (see [ROF92]) is adapted for denoising images corrupted by an additive white Gaussian noise. It consists in minimizing among $u \in \mathbb{N}^{\mathcal{P}}$

$$\beta TV(u) + \|u - v\|^2, \quad (9)$$

where the $TV(\cdot)$ operator is defined in (2). Observe that the functional (5) is the same than (9) when $K = 1$ and w_1 tends to infinity. This situation corresponds to a single Gaussian function of an infinite size. Let us now consider the following shape optimization problem for a fixed level $\mu \in \mathbb{R}$: We minimize among $\hat{u} \in \{0, 1\}^{\mathcal{P}}$

$$\beta TV(\hat{u}) + 2 \sum_{p \in \mathcal{P}} \left(\hat{u}_p \left(\mu - \frac{1}{2} \right) + v_p (1 - \hat{u}_p) \right). \quad (10)$$

In the next paragraph, we will denote by u^* the minimizer of (9) and \hat{u}_{μ}^* the minimizer of (10), for any level $\mu \in \mathbb{R}$.

The connection between the problems (9) and (10) is discussed in [Cha05]¹. Chambolle states that, for any level $\mu \in \mathbb{R}$, the μ level-set of the minimizer u^* of (9) (i.e. $\mathbf{1}_{\{u^* \geq \mu\}}$, where $\mathbf{1}_{\{\cdot\}}$ is

¹The same results were independently obtained by Darbon and Sigelle in a probabilistic setting [DS04].

the indicator function which returns one if its argument is true and zero otherwise) is a minimizer of (10). Conversely, the minimizer \hat{u}_μ^* of (10) is a μ level-set of the minimizer of (9). These statements notably mean that (9) can be minimized by independently solving an appropriate family of binary problems (10). For any levels $\mu_1, \mu_2 \in \mathbb{N}$ such that $\mu_1 < \mu_2$, one can easily see that $\hat{u}_{\mu_2}^* \leq \hat{u}_{\mu_1}^*$ [Cha05, DS04]. Using this monotone property, the minimizer u^* of (9) can therefore be constructed from the whole family of minimizers \hat{u}_μ^* of (10) by setting for each pixel $p \in \mathcal{P}$

$$u_p^* = \sup \{ \mu \in \mathbb{N} : \hat{u}_\mu^*(p) = 1 \}.$$

Given the form of $TV(\hat{u}_\mu)$ (see (2)), it is straightforward to see that the inequality (8) in Section 3.2 holds for any binary problem (10). The functional (9) can therefore be minimized in polynomial time using graph cuts for each binary problem (10). This is a particular case of [DS06] which presents a generalization of this idea to any convex data fidelity term.

These observations lead to an algorithmic scheme with a worst-case complexity of $O(T(\#\mathcal{V}, \#\mathcal{E})l_{max})$ where $T(\#\mathcal{V}, \#\mathcal{E})$ is the complexity of the max-flow algorithm used and $l_{max} = \max_p \{u_p\} \leq 2^\rho - 1$ is the maximum intensity² of the image u .

Nevertheless, such an approach is particularly time consuming when ρ is large. As observed in [DS04, Cha05], a pixel only needs to be involved in $O(\log_2(l_{max}))$ computations since it is useless to take into account pixels which are greater than μ for optimizations which only deal with pixels lesser or equal than μ , and conversely. A dyadic scheme leveraging this observation is proposed in [DS04, Cha05]. Compared to [Cha05], this complexity is improved in [DS04] by separating and processing independently the connected components of each binary solution. A slightly faster algorithm is obtained in [CD09] by reusing the flow found for a given level for the next level by dynamically updating the edge weights in the same graph. This is made possible in our situation since the set of nodes connected to the source s is growing as the level μ increases (see [CD09]).

Let us now describe how to solve the first step of Table 3 using the technique described in [Cha05, DS04]. We assume that the parameters $(\theta_k)_{1 \leq k \leq K}$ of the Gaussians shots are known. Notice that the third and fourth terms in (5) are irrelevant since they do not depend on u . We are therefore interested in minimizing, among $u \in \mathbb{N}^{\mathcal{P}}$

$$\beta TV(u) + \frac{1}{2\sigma^2} \|M_{(\theta_k)_{1 \leq k \leq K}} u - v\|^2. \quad (11)$$

Let us start by expanding (11) using (4)

$$\begin{aligned} & \beta TV(u) + \frac{1}{2\sigma^2} \|M_{(\theta_k)_{1 \leq k \leq K}} u - v\|^2 \\ = & \beta TV(u) + \frac{1}{2\sigma^2} \sum_{p \in \mathcal{P}} \sum_{k=1}^K (G_{\theta_k}(p) u_p - v_p^k)^2 \\ = & \beta TV(u) + \frac{1}{2\sigma^2} \sum_{p \in \mathcal{P}} \sum_{k=1}^K (u_p - a_p^k)^2 G_{\theta_k}^2(p) \quad \text{with} \quad a_p^k = \frac{v_p^k}{G_{\theta_k}(p)}, \end{aligned} \quad (12)$$

Notice that no division by zero occurs in a_p^k since we trivially have $G_{\theta_k}(p) > 0$ for any Gaussian $k \in \{1, \dots, K\}$ and any pixel $p \in \mathcal{P}$. In what follows, we first remind how to formulate $TV(\cdot)$ and

²The value of ρ is typically 8 or 16 in this setting.

the data fidelity term in (12) through level-sets. Let us start with the first one. For any pixel pair $(p, q) \in \mathcal{N}$, we can easily express $|u_p - u_q|$ in terms of level-sets over all possible grayscale intensities with

$$|u_p - u_q| = \sum_{\mu=0}^{l_{max}} |\mathbf{1}_{\{u_p \geq \mu\}} - \mathbf{1}_{\{u_q \geq \mu\}}|.$$

Together with (2), we obtain

$$\begin{aligned} TV(u) &= \sum_{\mu=0}^{l_{max}} \sum_{(p,q) \in \mathcal{N}} d_q^p |\mathbf{1}_{\{u_p \geq \mu\}} - \mathbf{1}_{\{u_q \geq \mu\}}| \\ &= \sum_{\mu=0}^{l_{max}} TV(\mathbf{1}_{\{u \geq \mu\}}). \end{aligned} \quad (13)$$

Let us now express the data fidelity term of (12) through level-sets for a fixed Gaussian $k \in \{1, \dots, K\}$ and a pixel $p \in \mathcal{P}$. By using the facts that for any $b \in \mathbb{N}$, we have

$$\begin{aligned} (a - b)^2 &= (a + 1)^2 + \sum_{\mu=0}^b [(a - \mu)^2 - (a - (\mu - 1))^2] \\ &= (a + 1)^2 + 2 \sum_{\mu=0}^b \left[\mu - \frac{1}{2} - a \right] \\ &= (a + 1)^2 + 2 \sum_{\mu=0}^{l_{max}} \left[\mu - \frac{1}{2} - a \right] \mathbf{1}_{\{b \geq \mu\}}, \end{aligned} \quad (14)$$

and by using (14) in (12), we obtain (always for a fixed Gaussian $k \in \{1, \dots, K\}$ and a pixel $p \in \mathcal{P}$)

$$(u_p - a_p^k)^2 G_{\theta_k}^2(p) = G_{\theta_k}^2(p) \left[(a_p^k + 1)^2 + 2 \sum_{\mu=0}^{l_{max}} \left(\mu - \frac{1}{2} - a_p^k \right) \mathbf{1}_{\{u_p \geq \mu\}} \right].$$

Together with the data fidelity term as written in (12), this leads to

$$\begin{aligned} & \sum_{k=1}^K \sum_{p \in \mathcal{P}} G_{\theta_k}^2(p) \left[(a_p^k + 1)^2 + 2 \sum_{\mu=0}^{l_{max}} \left(\mu - \frac{1}{2} - a_p^k \right) \mathbf{1}_{\{u_p \geq \mu\}} \right] \\ &= C' + \sum_{k=1}^K \sum_{p \in \mathcal{P}} 2 G_{\theta_k}^2(p) \sum_{\mu=0}^{l_{max}} \left[\left(\mu - \frac{1}{2} \right) \mathbf{1}_{\{u_p \geq \mu\}} + a_p^k \mathbf{1}_{\{u_p < \mu\}} \right] \\ &= C' + \sum_{\mu=0}^{l_{max}} 2 \left(\sum_{k=1}^K \sum_{p \in \mathcal{P}} G_{\theta_k}^2(p) \left[\left(\mu - \frac{1}{2} \right) \mathbf{1}_{\{u_p \geq \mu\}} + a_p^k \mathbf{1}_{\{u_p < \mu\}} \right] \right), \end{aligned} \quad (15)$$

where C' does not depend on u . Using both $\mathbf{1}_{\{u_p \geq \mu\}}$ and $\mathbf{1}_{\{u_p < \mu\}}$ in the above formula is due to the graph construction illustrated in Figure 2. Finally, combining (13) with (15) and using (12) gives

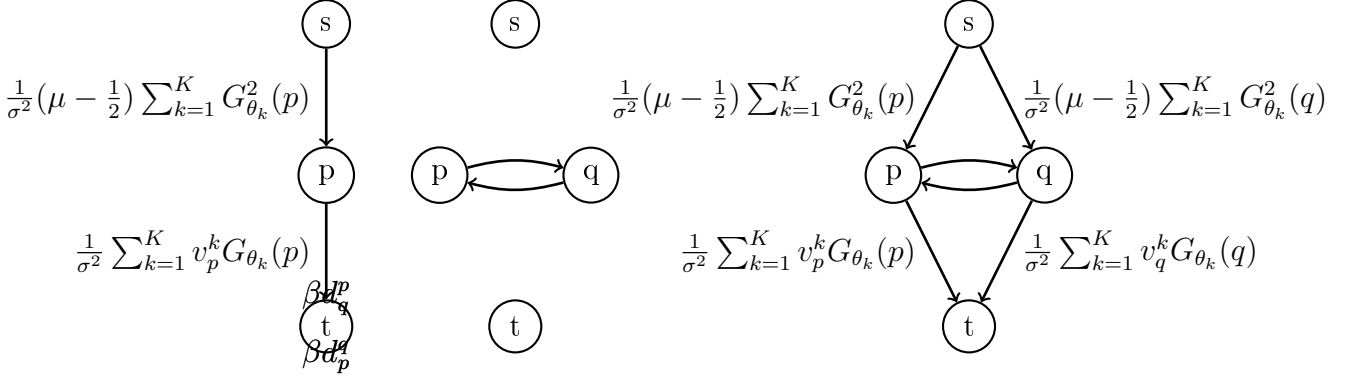


Figure 2: Networks representations for solving a binary problem (16) at a fixed level $\mu \in \mathbb{N}$. From left to right: the network representing the unary term E'_p of (16) for any pixel $p \in \mathcal{P}$, the network representing the pairwise term $E'_{p,q}$ for any pixel pair $(p, q) \in \mathcal{N}$ and the complete network combining the two previous ones. Under the relationship $\mathbf{1}_{\{u \geq \mu\}} \Leftrightarrow p \in \mathcal{S}$ and $\mathbf{1}_{\{u < \mu\}} \Leftrightarrow p \in \mathcal{T}$ (see (7) in Section 3.1), it is easy to see that for each configuration of $\mathbf{1}_{\{u \geq \mu\}}$ and $\mathbf{1}_{\{u < \mu\}}$, (16) is equal to the corresponding s-t cut for a particular value of μ .

the following discretizations (up to a constant C')

$$\begin{aligned}
& \beta TV(u) + \frac{1}{2\sigma^2} \|M_{(\theta_k)_{1 \leq k \leq K}} u - v\|^2 \\
&= \sum_{\mu=0}^{l_{max}} \left(\beta TV(\mathbf{1}_{\{u \geq \mu\}}) + \frac{1}{\sigma^2} \sum_{k=1}^K \sum_{p \in \mathcal{P}} G_{\theta_k}^2(p) \left[\left(\mu - \frac{1}{2} \right) \mathbf{1}_{\{u_p \geq \mu\}} + a_p^k \mathbf{1}_{\{u_p < \mu\}} \right] \right) \\
&= \sum_{\mu=0}^{l_{max}} \left(\beta TV(\mathbf{1}_{\{u \geq \mu\}}) + \frac{1}{\sigma^2} \sum_{p \in \mathcal{P}} \sum_{k=1}^K G_{\theta_k}^2(p) \left[\left(\mu - \frac{1}{2} \right) \mathbf{1}_{\{u_p \geq \mu\}} + \frac{v_p^k}{G_{\theta_k}(p)} \mathbf{1}_{\{u_p < \mu\}} \right] \right) \\
&= \sum_{\mu=0}^{l_{max}} \left(\underbrace{\beta \sum_{(p,q) \in \mathcal{N}} d_{pq}^p |\mathbf{1}_{\{u_p \geq \mu\}} - \mathbf{1}_{\{u_q \geq \mu\}}|}_{E'_{p,q}(\mathbf{1}_{\{u_p \geq \mu\}}, \mathbf{1}_{\{u_q \geq \mu\}})} + \underbrace{\sum_{p \in \mathcal{P}} \frac{1}{\sigma^2} \left[\left(\mu - \frac{1}{2} \right) \mathbf{1}_{\{u_p \geq \mu\}} \sum_{k=1}^K G_{\theta_k}^2(p) + \mathbf{1}_{\{u_p < \mu\}} \sum_{k=1}^K v_p^k G_{\theta_k}(p) \right]}_{E'_p(\mathbf{1}_{\{u \geq \mu\}})} \right). \quad (16)
\end{aligned}$$

It is now straightforward to see that the latter equation has the same form as (10) and can therefore be minimized using the same approach as in [Cha05, DS04].

The remaining of this section is to construct a capacitated network for any level $\mu \in \mathbb{N}$ such that there is a one-to-one correspondence between s-t cuts and $\mathbf{1}_{\{u \geq \mu\}}$ and thus between the capacity of the s-t cut and $f(u, (\theta_k)_{1 \leq k \leq K})$. In that case, such a network is called graph-representable (see [KZ04]). Following the methodology of [KZ04], one can easily construct for any pixel $p \in \mathcal{P}$, a network for the terms $E'_p(\cdot)$ and $E'_{p,q}(\cdot, \cdot)$ appearing in (16). These networks are depicted in Figure 2. Using the additivity theorem of [KZ04], one can now combine these two networks into a single one by adding their common edge capacities.

4 The estimate of the Gaussian parameters

In this section, we provide the details useful for the implementation of a gradient descent algorithm with an Armijo step size rule (see [Ber03]) solving the step 2 of the algorithm described in Table 3.

Before giving the formula of the gradient of f , let us remind the notation $c_k = (c_{k,i}, c_{k,j}) \in \mathbb{R}^2$ and $p = (p_i, p_j) \in \mathcal{P}$.

For $v \in \mathbb{R}^{K\mathcal{P}}$, $u \in \mathbb{R}^{\mathcal{P}}$ and $(c_k, w_k)_{1 \leq k \leq K} \in \mathbb{R}^{3K}$, we obtain after some calculation

$$\frac{\partial f}{\partial c_{k,i}} = \frac{c_{k,i} - \bar{c}_{k,i}}{\sigma_c^2} + \frac{1}{\sigma^2 w_k^2} \sum_{p \in \mathcal{P}} (p_i - c_{k,i}) e^{-\frac{\|p - c_k\|^2}{2w_k^2}} u_p \left[e^{-\frac{\|p - c_k\|^2}{2w_k^2}} u_p - v_p^k \right],$$

$$\frac{\partial f}{\partial c_{k,j}} = \frac{c_{k,j} - \bar{c}_{k,j}}{\sigma_c^2} + \frac{1}{\sigma^2 w_k^2} \sum_{p \in \mathcal{P}} (p_j - c_{k,j}) e^{-\frac{\|p - c_k\|^2}{2w_k^2}} u_p \left[e^{-\frac{\|p - c_k\|^2}{2w_k^2}} u_p - v_p^k \right],$$

and

$$\frac{\partial f}{\partial w_k} = \frac{w_k - \bar{w}_k}{\sigma_w^2} + \frac{1}{\sigma^2 w_k^3} \sum_{p \in \mathcal{P}} \|p - c_k\|^2 e^{-\frac{\|p - c_k\|^2}{2w_k^2}} u_p \left[e^{-\frac{\|p - c_k\|^2}{2w_k^2}} u_p - v_p^k \right].$$

The stopping criterion of the gradient descent algorithm controls that the variation of $(\theta_k)_{1 \leq k \leq K}$, between two successive iterations is smaller than a parameter ε_e . To avoid losing too much time during the first estimations of the algorithm described in Table 3, we choose to express ε_e in terms of the iteration number n with

$$\varepsilon_e = (\varepsilon_e^{max} - \varepsilon_e^{min}) \cdot \exp\left(-\frac{n}{\sigma_{\varepsilon_e}}\right) + \varepsilon_e^{min},$$

where the parameters ε_e^{min} , ε_e^{max} and σ_{ε_e} are empirically set (see Section 5). In words, the accuracy of the estimation is larger when the iteration number increases.

5 Numerical experiments

5.1 Applicative framework

The camera is made of an optical system and a typical 256×256 pixels focal plane array (i.e. $N = 256$). As already mentioned, for low signal levels, we consider that the additive Gaussian thermal noise dominates. We consider several noise levels reflecting different possible illumination levels: $\sigma = 0.05, 0.1, 0.2$ and 0.4 . Notice that the pixel intensity in the ideal observed image ranges between 0 and 1.

The field of view of the camera is $FoV = 8.5 \text{ mrad}$. The laser source is a typical fiber laser, with beam quality factor close to 1, combined with a collimator and a deflection device. The laser beam illuminates a solid angle corresponding to a Gaussian beam of 1.08 mrad in divergence. Its expected radius is $\bar{w}_k = 16.2$ pixels in the image. The standard deviation around this radius is typically of $\sigma_w = 0.07$ pixels (see Table 1). From laser shot to laser shot, the nominal beam axis is deviated over a regular grid of dimension $K = 9 \times 9$. After atmospheric perturbations, the expected location \bar{c}_k of

the beam axis belongs to (in pixels)

$$\bar{c}_k \in \left\{ \frac{N}{18}, \frac{N}{18} + \frac{N}{9}, \dots, \frac{N}{18} + 8\frac{N}{9} \right\}^2.$$

The standard deviation around this expected value is typically of $\sigma_c = 0.81$ pixels (see Table 2).

5.2 Implementation details

In the following experiments, the max-flow implementation v3.0 of [BK04] is used. Finally, a Moore neighborhood is considered for each pixel p on the lattice \mathcal{P} , i.e. involving all pixels whose Euclidean distance from p is less or equal to $\sqrt{2}$ pixels. The minimization is implemented with a dyadic parametric scheme and typically represents 10 percent of the overall computations. **In the step of estimating Gaussian parameters, we empirically set $\varepsilon_e^{min} = 0.005$, $\varepsilon_e^{max} = 0.5$ and $\sigma_{\varepsilon_e} = 2.0$.**

Nevertheless, our implementation is not optimized and we do not provide detailed computing times since we do not believe they are indicative of the computing time for an optimized version of these algorithms. In particular, a simple improvement with this regard would consist in extracting from each image v^p a small window containing the laser shot. Many computations could also be parallelized. With the current implementation, the restoration of an image of size 256×256 from 81 laser shots requires between 3 minutes and 20 seconds on a computer whose processor is clocked at 3.47GHz.

5.3 Measuring the influence of the parameters

This section focuses on how the parameters β and \bar{w}_k affect the quality of the image estimate in the algorithm with an additive white Gaussian noise of standard deviation $\sigma = 0.1$. An example of reconstruction is illustrated in Figure 3 for the “lena” image with a varying amount of regularization. To better visualize the available data, laser and Gaussian shots are each gathered into a single image where a pixel is assigned with its maximum intensity over all $1 \leq k \leq K$. In order to illustrate the influence of β , we also set the other parameters in such a way that the center and the spread of Gaussians do essentially not vary. We therefore set $\sigma_c = 0.0001$, $\sigma_w = 0.0001$ and $\bar{w}_k = 30$, $\forall 1 \leq k \leq K$. Due to the particular values of these parameters and the level of accuracy ε_a , we have $w_k \simeq \bar{w}_k$ and $c_k \simeq \bar{c}_k$, $\forall 1 \leq k \leq K$. Thus, the algorithm only consists of a single iteration **for the global loop**.

The strength of the regularization grows with β . This is consistent with the equation (11) since this parameter is attached to the regularization term. The parameter β therefore needs to be adequately tuned to remove noise without losing too much details. Also, as expected when β increases, the result progressively becomes a cartoon-like image with sharp boundaries surrounded by large and flat regions. In particular, textures and thin details tend to disappear. Due to the proximity to the TV+ L^2 model, we also observe its usual side-effects: staircasing and loss of contrast.

Finally, the Figure 4 illustrates the effect of varying the parameter \bar{w}_k on the “man” image. Partial available data through laser shots is represented on the top row, in the same way as in Figure 3. The obtained results are depicted for $\bar{w}_k = 6$, $\bar{w}_k = 9$, $\bar{w}_k = 12$ and $\bar{w}_k = 20$. The parameters σ_c , σ_w , and

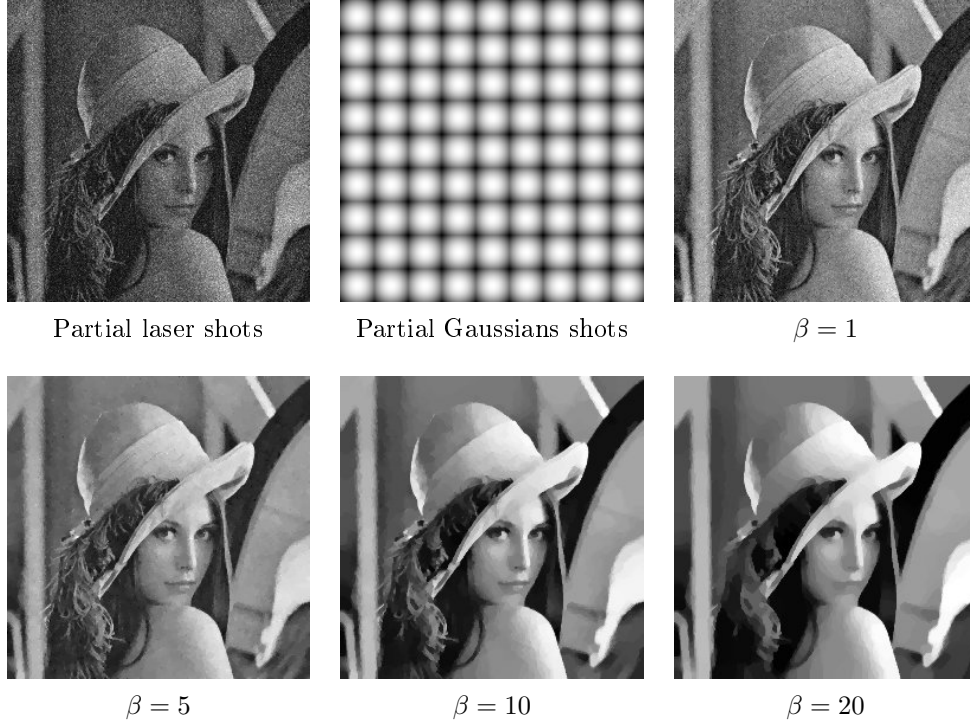


Figure 3: Influence of the regularization parameter β on the “lena” image. Each pixel of the top left image is assigned with its maximum intensity over all laser shots. Similarly, each pixel on the middle top view is assigned with the maximum illumination intensity over all laser shots. In this experiment, we set $\sigma_c = 0.0001$, $\sigma_w = 0.0001$, $\sigma = 0.1$ and $\bar{w}_k = 30$, $\forall 1 \leq k \leq K$.

σ are set with the same values as in the Figure 3. As expected, when \bar{w}_k is small (i.e. when Gaussians correspond to small spots), the reconstruction is of poor quality and details of the image cannot be accurately recovered between Gaussians. Indeed, for such pixels, the missing data is too important and their intensities are assigned by the regularization. Nevertheless, a better quality reconstruction can be reached when \bar{w}_k is larger.

5.4 Convergence of $(\theta_k)_{1 \leq k \leq K}$

In this section, we empirically demonstrate the convergence of the reconstruction algorithm in Figure 5 for four levels of noise and eight grayscale images. For each noise level, we measure the distance between the estimated parameters θ^n obtained at iteration n of the algorithm in Table 3 and the true parameters θ^* with

$$(\|\theta^n - \theta^*\|)_{n \in \mathbb{N}} = (\|c_i^n - c_i^*\| + \|c_j^n - c_j^*\| + \|w^n - w^*\|)_{n \in \mathbb{N}}. \quad (17)$$

In this experiment, we set $\bar{w}_k = 16.2$, $\sigma_c = 0.81$, $\sigma_w = 0.07$. Additionally, the penalty parameter β is hand-tuned and set according to the noise level (see Table 4), independently of the image. As expected, we see that the distance (17) strongly decreases for all images in the first iterations and becomes relatively stable in the following iterations. This means that the image estimate is mainly improved at the beginning of the algorithm. In particular, we see that the number of iterations of the latter could be reduced by slightly relaxing the parameter ε_a . We also observe that the average

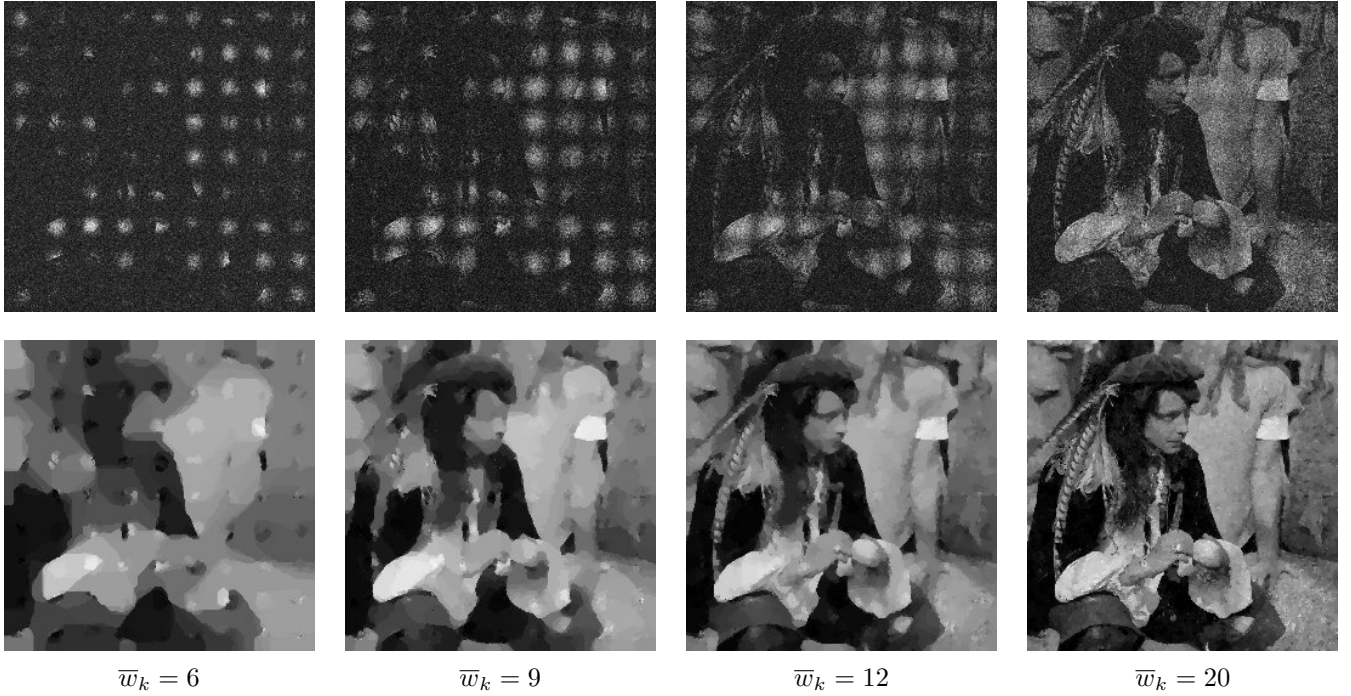


Figure 4: Influence of the parameter \bar{w}_k on the “man” image with $\beta = 3.0$. On top row, each pixel of the images is assigned with its maximum intensity over all laser shots. The remaining parameters σ_c , σ_w and σ are set with the same values as in Figure 3. Notice that we target $\bar{w}_k = 16.2$ for our application (see Section 5.5).

Noise level σ	0.05	0.1	0.2	0.4
Corresponding β	5	2.3	1.5	0.8

Table 4: Correspondence between the noise level and the parameter β .

number of iterations is smaller and the decrease of (17) is less important when the amount of noise σ increases. Notice finally that the estimation of the parameters is fairly robust to the observed scene.

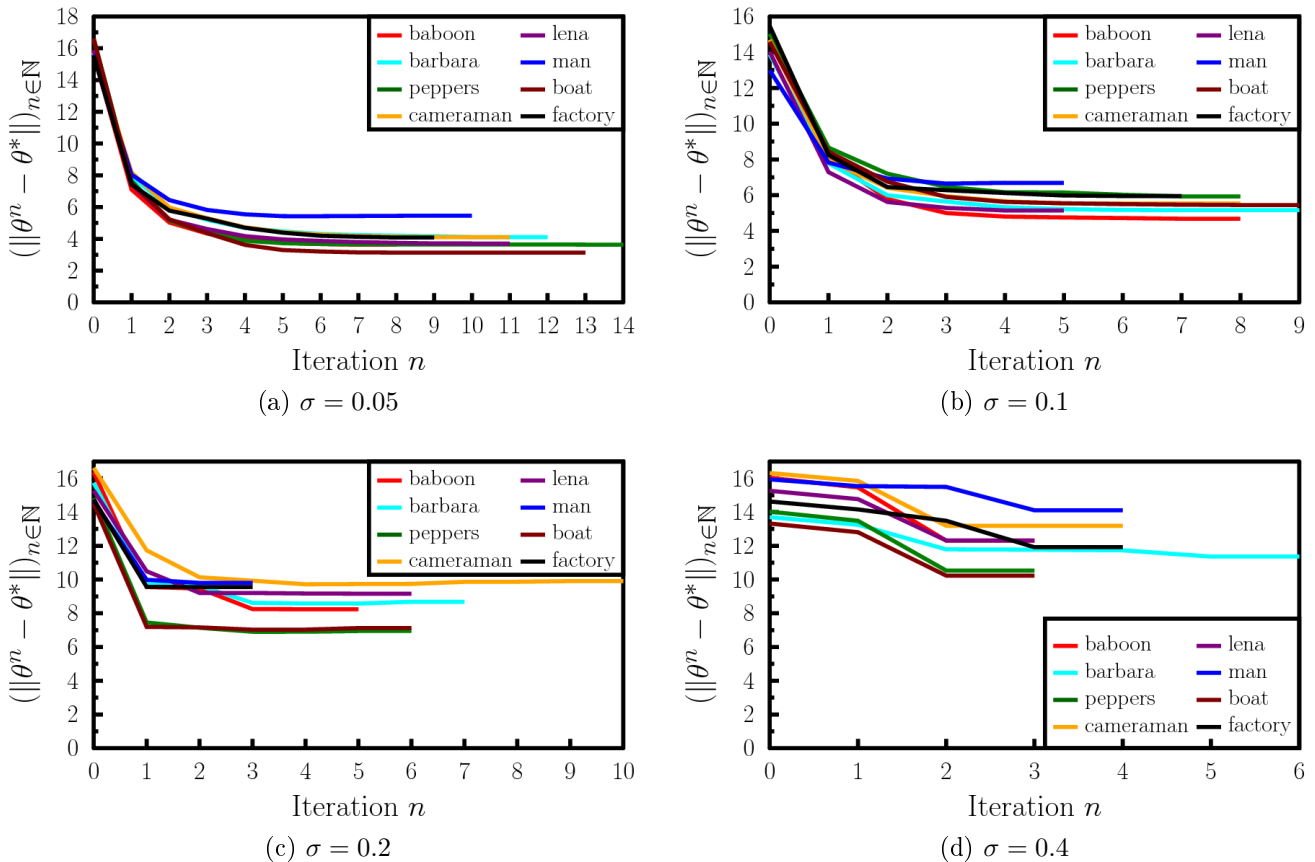


Figure 5: Convergence of the reconstruction algorithm for four different noise levels. On each figure, the distance $(\|\theta^n - \theta^*\|)_{n \in \mathbb{N}}$ (see equation (17)) between the estimated parameters θ^n and the true parameters θ^* is represented as a function of the iteration n . This experiment is for $\bar{w}_k = 16.2$, $\sigma_c = 0.81$, $\sigma_w = 0.07$. The regularization parameter β is tuned by hand.

5.5 Accuracy

In this section, we study the quality of the image estimate as well as the performance of the reconstruction algorithm with a varying amount of noise σ and on the same images as in Section 5.4. For each level of noise, we generate noisy data according to this level and run the reconstruction algorithm. Then, we measure the quality between the noise-free image and the restored image using two metrics: PSNR (Peak Signal-to-Noise Ratio) and MSE (Mean Square Error)³. **Also, the gray levels range between 0 and 1 in all the considered images.**

The parameters β , σ_c , σ_w and \bar{w}_k are set with the same values as in Section 5.4. The results of these experiments are summarized in Table 5 and illustrated in the Figures 6, 7, 8 and 9 for $\sigma = 0.05$, $\sigma = 0.1$, $\sigma = 0.2$ and $\sigma = 0.4$, respectively.

³These measures are described at <http://megawave.cmla.ens-cachan.fr/stuff/guid3/node256.html#fmse>.

Let us now analyze the obtained results. For a moderate level of noise ($\sigma = 0.05$ and $\sigma = 0.1$), the algorithm behaves well: large flat areas are well denoised; thin structures and textures are well preserved even between Gaussian laser illumination domes where the knowledge about data is more uncertain (see e.g. the “barbara” image and the “factory” image in Figure 7). The latter point is important and is due to the fact that the Gaussian illumination domes are not too far from each other in our application. For a larger level of noise ($\sigma = 0.2$ and $\sigma = 0.4$), large flat areas are well smoothed yet (see e.g. the “cameraman” image in Figure 8) but textures disappear in the residues (see e.g. the face in the “man” image of Figure 9). These observations are also confirmed by the increase of the MSE and the decrease of the PSNR for all images in Table 5. Also, an important point is that we choose to keep undesired and isolated pixels in Figure 9. Such pixels could be easily removed by increasing β but would oversmooth the image estimate.

6 Conclusion

blabla

References

- [BBFAC04] J. Bect, L. Blanc-Féraud, G. Aubert, and A. Chambolle. A L1-unified variational framework for image restoration. *Lecture Notes in Computer Science*, 3024:1–13, 2004. Proceedings of European Conference on Computer Vision 2004.
- [Ber03] D.P. Bertsekas. *Nonlinear Programming*. Athena Scientific, second edition, 2003.
- [BK04] Y. Boykov and V. Kolmogorov. An experimental comparison of min-cut/max-flow algorithms for energy minimization in vision. *Pattern Analysis And Machine Intelligence*, 26(9):1124–1137, 2004.
- [BK05] Y. Boykov and V. Kolmogorov. Computing geodesics and minimal surfaces via graph cuts. In *International Conference on Computer Vision*, volume 1, pages 26–33, October 2005.
- [CD09] A. Chambolle and J. Darbon. On total variation minimization and surface evolution using parametric maximum flows. *International Journal of Computer Vision*, 84(3):288–307, 2009.
- [Cha92] F. Chassat. *Optical propagation through atmospheric turbulence: moral study and application of anisoplanatism in adaptive optics*. PhD thesis, University of Paris Sud, 1992.
- [Cha04] A. Chambolle. An algorithm for total variation minimization and applications. *Journal of Mathematical Imaging and Vision*, 20(1-2):89–97, January-March 2004.

Noise level	Image name	MSE	PSNR
$\sigma = 0.05$	baboon	0.0023	25.7
	barbara	0.0015	27.6
	peppers	0.0008	30.7
	cameraman	0.0008	30.8
	lena	0.0008	30.5
	man	0.0014	28.5
	boat	0.0012	29.3
	factory	0.0011	29.6
$\sigma = 0.1$	baboon	0.0051	22.3
	barbara	0.0034	24.0
	peppers	0.0020	26.7
	cameraman	0.0020	26.8
	lena	0.0020	26.4
	man	0.0031	25.0
	boat	0.0027	25.7
	factory	0.0025	25.9
$\sigma = 0.2$	baboon	0.0092	19.7
	barbara	0.0062	21.4
	peppers	0.0039	23.8
	cameraman	0.0040	23.9
	lena	0.0038	23.8
	man	0.0061	22.1
	boat	0.0051	22.9
	factory	0.0046	23.3
$\sigma = 0.4$	baboon	0.0134	18.0
	barbara	0.0102	19.3
	peppers	0.0079	20.7
	cameraman	0.0080	20.8
	lena	0.0076	20.7
	man	0.0108	19.6
	boat	0.0092	20.4
	factory	0.0084	20.6

Table 5: Accuracy of the reconstruction algorithm on several grayscale images with a varying amount of noise σ . In this experiment, we set $\sigma_c = 0.81$, $\sigma_w = 0.07$, $\bar{w}_k = 16.2$ and tune the regularization parameter β by hand.

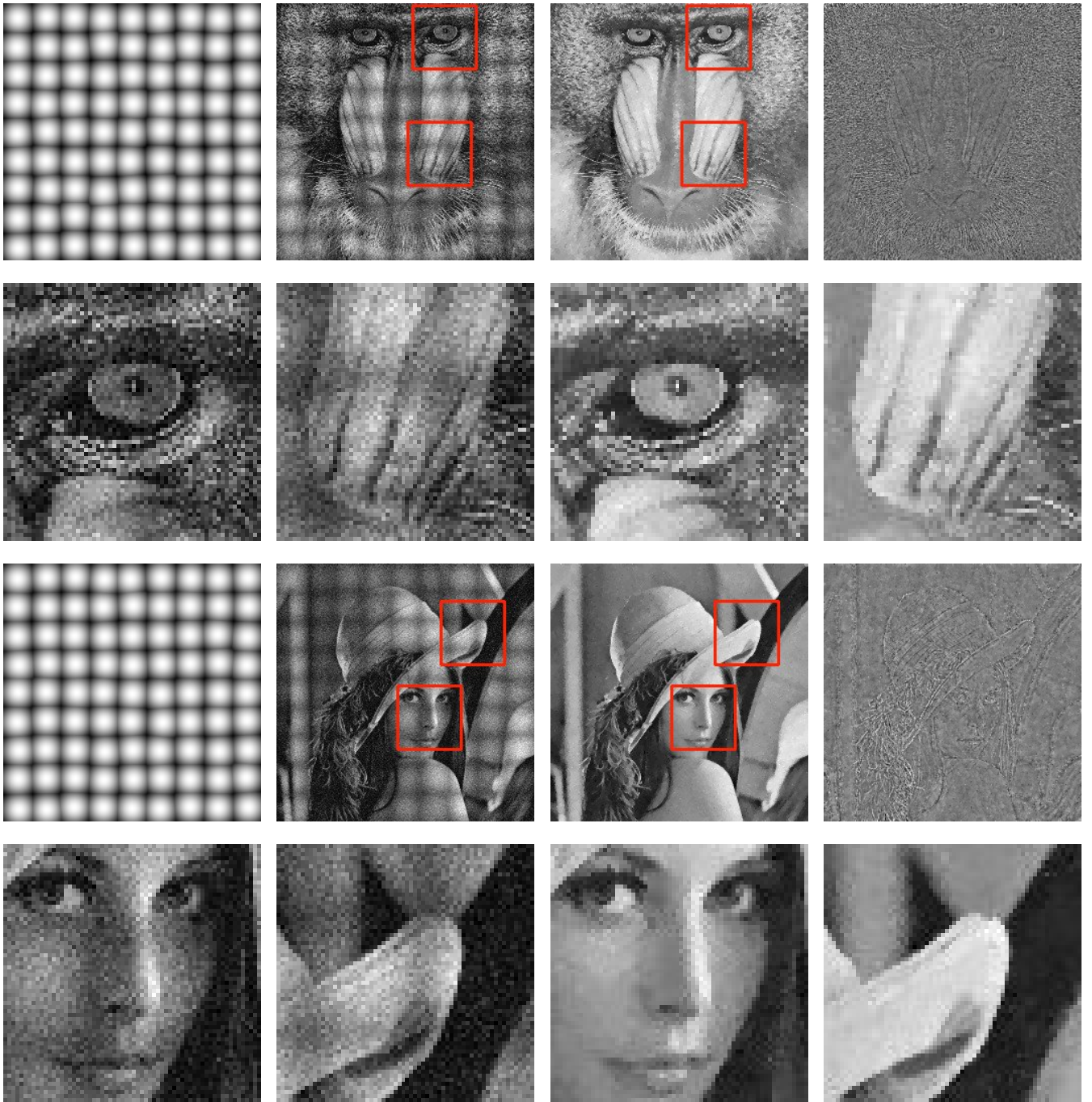


Figure 6: From top to bottom: reconstruction of the images “baboon” (first and second rows) and “lena” (third and fourth rows) with $\sigma = 0.05$. The leftmost and left images of the first and third rows correspond resp. to the Gaussian laser illumination domes and to the partial available data, represented in the same way than in Figure 3. The remaining images on these rows resp. correspond to the image estimate and the error between the estimated and the ideal image. Detailed views of partial laser shots (leftmost and left images) and the image estimate (right and rightmost images) are provided on the second and fourth rows. Here, we set $\bar{w}_k = 16.2$, $\sigma_c = 0.81$, $\sigma_w = 0.07$ and $\beta = 5.0$.

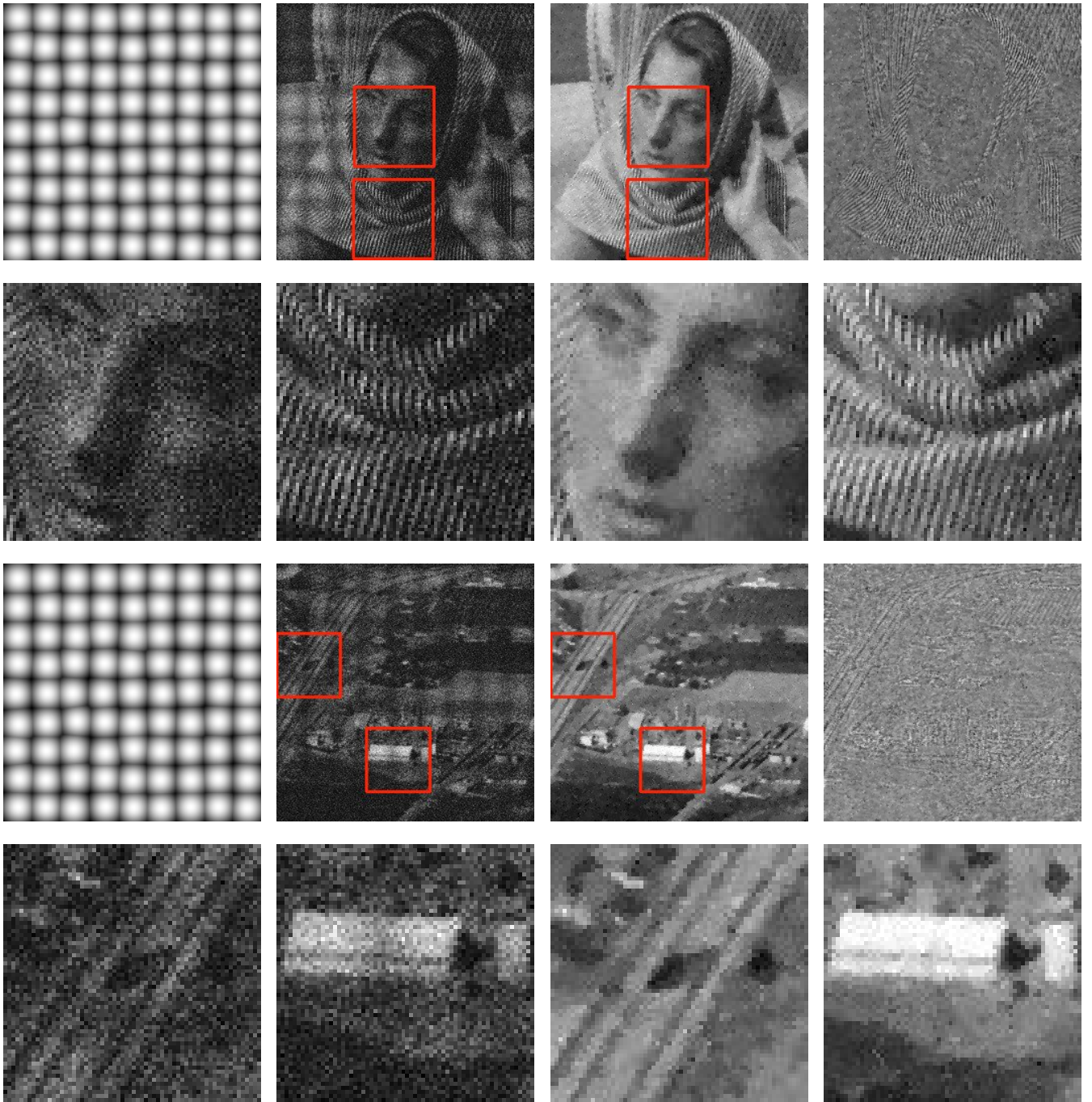


Figure 7: From top to bottom: reconstruction of the images “barbara” (first and second rows) and “factory” (third and fourth rows) with $\sigma = 0.1$. The leftmost and left images of the first and third rows correspond resp. to the Gaussian laser illumination domes and to the partial available data, represented in the same way as in Figure 3. The remaining images on these rows resp. correspond to the image estimate and the error between the estimated and the ideal image. Detailed views of partial laser shots (leftmost and left images) and the image estimate (right and rightmost images) are provided on the second and fourth rows. Here, we set $\bar{w}_k = 16.2$, $\sigma_c = 0.81$, $\sigma_w = 0.07$ and $\beta = 2.3$.

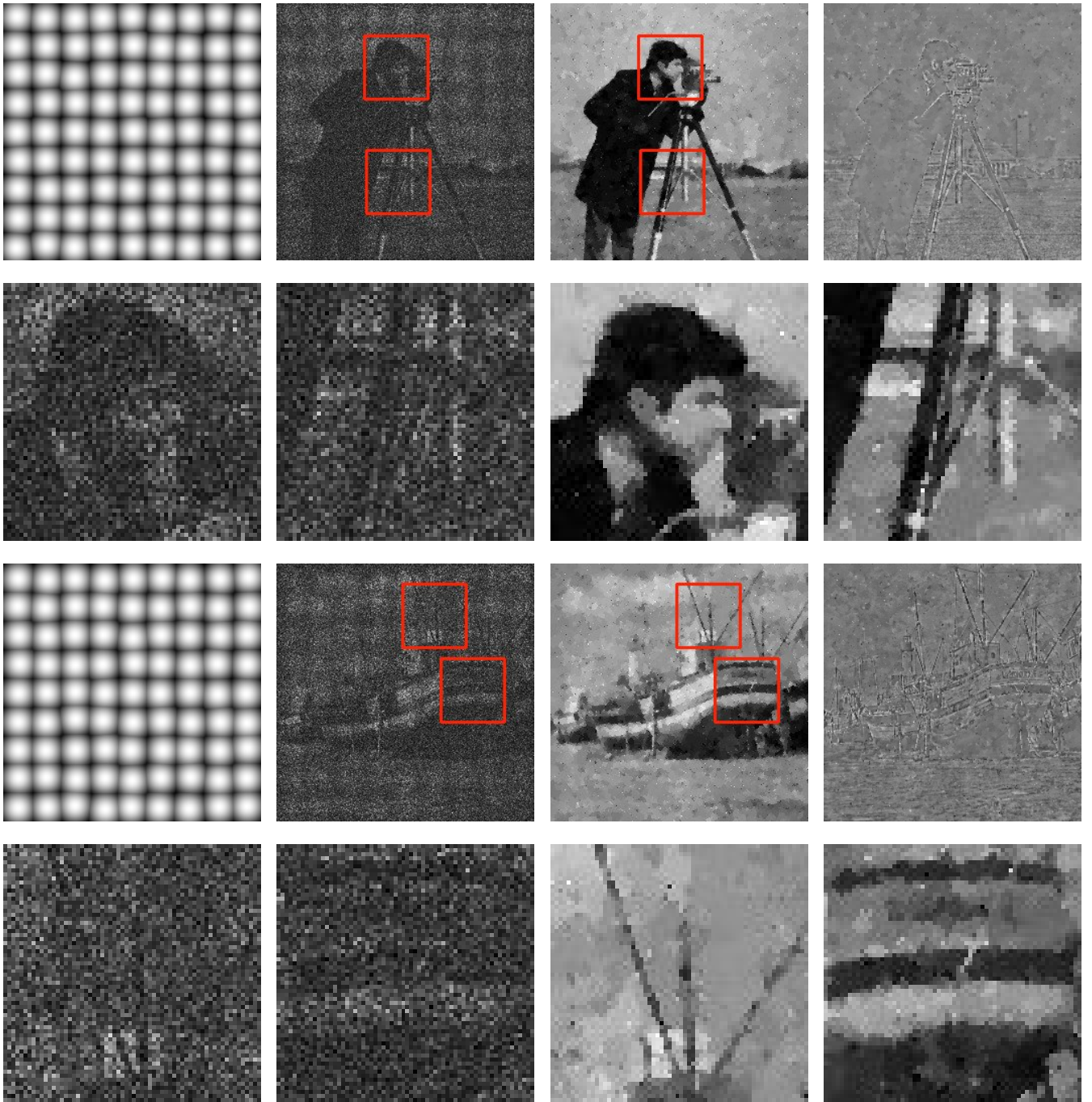


Figure 8: From top to bottom: reconstruction of the images “cameraman” (first and second rows) and “boat” (third and fourth rows) with $\sigma = 0.2$. The leftmost and left images of the first and third rows correspond resp. to the Gaussian laser illumination domes and to the partial available data, represented in the same way than in Figure 3. The remaining images on these rows resp. correspond to the image estimate and the error between the estimated and the ideal image. Detailed views of partial laser shots (leftmost and left images) and the image estimate (right and rightmost images) are provided on the second and fourth rows. Here, we set $\bar{w}_k = 16.2$, $\sigma_c = 0.81$, $\sigma_w = 0.07$ and $\beta = 1.5$.

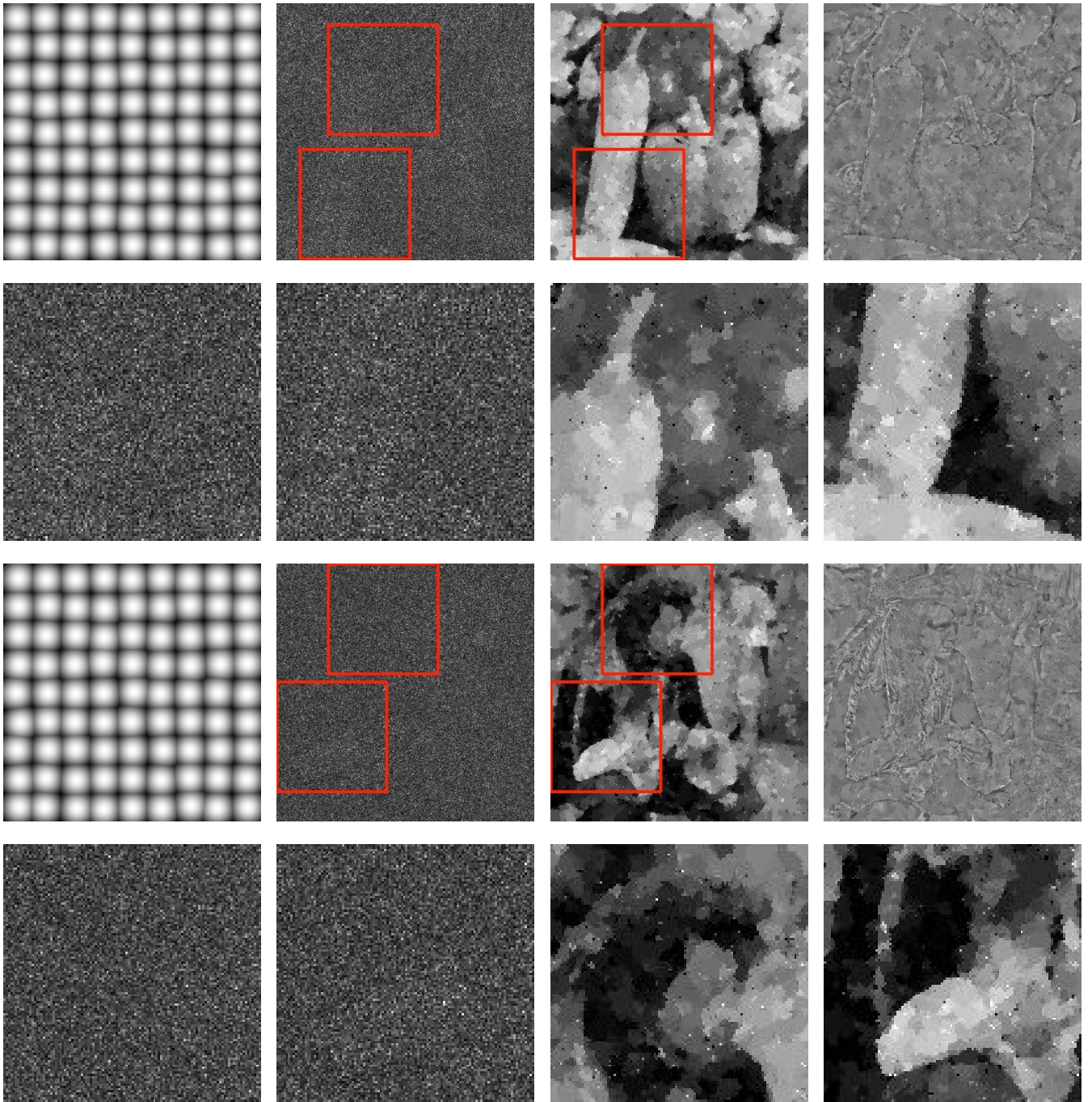


Figure 9: From top to bottom: reconstruction of the images “peppers” (first and second rows) and “man” (third and fourth rows) with $\sigma = 0.4$. The leftmost and left images of the first and third rows correspond resp. to the Gaussian laser illumination domes and to the partial available data, represented in the same way than in Figure 3. The remaining images on these rows resp. correspond to the image estimate and the error between the estimated and the ideal image. Detailed views of partial laser shots (leftmost and left images) and the image estimate (right and rightmost images) are provided on the second and fourth rows. Here, we set $\bar{w}_k = 16.2$, $\sigma_c = 0.81$, $\sigma_w = 0.07$ and $\beta = 0.8$.

- [Cha05] A. Chambolle. Total variation minimization and a class of binary MRF models. In *Lecture Notes in Computer Science, Energy Minimization Methods in Computer Vision and Pattern Recognition*, volume 3757, pages 136–152. Springer, 2005.
- [DS04] J. Darbon and M. Sigelle. Exact optimization of discrete constrained total variation minimization problems. In *International Workshop on Combinatorial Image Analysis*, volume 3322, pages 548–557. Klette, R. and Zunic, J., editors, December 2004.
- [DS06] J. Darbon and M. Sigelle. Image restoration with discrete constrained total variation part I: Fast and exact optimization. *Journal of Mathematical Imaging and Vision*, 26(3):261–276, 2006.
- [Fan75] R.L. Fante. Electromagnetic beam propagation in turbulent media. *Proceedings of the IEEE*, 63(12):1669–1692, December 1975.
- [Fri66] D.L. Fried. Optical resolution through a randomly inhomogeneous medium for very long and very short exposures. *Journal of the Optical Society of America*, 56(10):1372–1379, October 1966.
- [GPS89] D.M. Greig, B.T. Porteous, and A.H. Seheult. Exact maximum a posteriori estimation for binary images. *Journal of the Royal Statistical Society*, 51(2):271–279, 1989.
- [Ham10] D. Hamoir. Procédé et système d'imagerie active à champ large : Method and system for active imaging with a large field. Patent WO 2010119225, October 2010.
- [HVB⁺09] L. Hespel, M.-T. Velluet, A. Bonnefois, N. Rivière, M. Fracès, D. Hamoir, B. Tanguy, B. Duchenne, and J. Isbert. Comparison of a physics-based BIL simulator with experiments. In *Society of Photo-Optical Instrumentation Engineers, International Symposium on Photoelectronic Detection and Imaging*, volume 7382, page 73822T, June 2009.
- [Kol49] A.N. Kolmogorov. The local structure of turbulence in incompressible viscous fluid for very large Reynolds numbers. *Doklady Akademii Nauk SSSR*, 66(4):825, 1949. English translation in "Turbulence: Classic papers on statistical theory", edited by S. K. Friedlander and L. Topper (Interscience Publishers, Inc., New York, 1961), p. 151, 1961.
- [KZ04] V. Kolmogorov and R. Zabih. What energy functions can be minimized via graph cuts? *Pattern Analysis And Machine Intelligence*, 26(2):147–159, 2004.
- [RHV⁺09] N. Rivière, L. Hespel, M.-T. Velluet, Y.-M. Frédéric, P. Barillot, and F. Hélias. Modelling of an active burst illumination imaging system. In *Society of Photo-Optical Instrumentation Engineers, International Symposium on Photoelectronic Detection and Imaging*, volume 7382, pages 73822S–10, June 2009.
- [Rod81] F. Roddier. The effects of atmospheric turbulence in optical astronomy. *Progress in Optics*, 19:281–376, 1981.
- [ROF92] L.I. Rudin, S. Osher, and E. Fatemi. Nonlinear total variation based noise removal algorithms. *Physica D*, 60:259–268, 1992.